small structures
www.small-structures.com

Cu–O/N Single Sites Incorporated 2D Covalent Organic Framework Ultrathin Nanobelts for Highly Selective Visible-Light-Driven CO_2 Reduction to CO

Wenguang Tu, Yanqin Yang, Chunping Chen, Tianhua Zhou, Tianhao Li, Haojing Wang, Shuyang Wu, Yong Zhou, Dermot O'Hare, Zhigang Zou, and Rong Xu**

Developing heterogeneous catalysts with identifiable catalytic sites provides opportunities to explore their structure–activity relationship. Covalent organic framework (COF) represents an emerging class of porous materials that have exhibited great potential in various applications. Herein, a single-site heterogeneous photocatalyst consisting of 2D COF ultrathin nanobelts coordinated with single Cu–O/N sites (defined as Cu–COF) is synthesized and investigated for visible-light-driven CO_2 reduction. The relatively weak N and O binding sites from the imine and methoxy groups of the organic linkers result in active Cu–O/N sites for charge transfer and CO_2 reduction. The resultant Cu–COF with 0.2 wt% Cu only serves as a bifunctional photocatalyst for visible-light-driven CO_2 reduction in the absence of a photosensitizer with triethanolamine as the sacrificial reagent. A high CO selectivity of 94% is obtained. This study further demonstrates the great potential of COFs in heterogeneous catalysis with the abundant choices of functional groups in the organic linkers.

1. Introduction

Solar-driven reduction of CO_2 to value-added chemicals and fuels via artificial photosynthesis is one of the outstanding long-term solutions to reduce carbon emissions.[1–4] To gain high conversion efficiency and selectivity of CO_2 photoreduction, a series of heterogeneous semiconductor photocatalysts such as TiO_2,[5–8] CdS,[9–11] $ZnGe_2O_4$,[12,13] and $CsPbBr_3$[14,15] have been investigated. However, there exist many challenges to be overcome to achieve great improvement in CO_2 reduction rate and product selectivity, such as poor CO_2 adsorption, fast recombination of photogenerated charge carriers, and inactive surface sites.[16,17] To design more active and selective catalytic sites, molecularly defined crystalline solid structures such as metal–organic frameworks (MOFs) and covalent organic frameworks (COFs) offer great advantages for understanding the nature of

W. Tu, Y. Yang, H. Wang, S. Wu, R. Xu
School of Chemistry
Chemical Engineering and Biotechnology
Nanyang Technological University
62 Nanyang Drive, Singapore 637459, Singapore
E-mail: rxu@ntu.edu.sg

W. Tu, T. Li, Z. Zou
School of Science and Engineering
The Chinese University of Hong Kong
Shenzhen, Guangdong 518172, P.R. China
E-mail: zouzhigang@cuhk.edu.cn

Y. Yang
School of Chemical Engineering and Technology
Hebei University of Technology
Tianjin 300130, P.R. China

The ORCID identification number(s) for the author(s) of this article can be found under https://doi.org/10.1002/sstr.202200233.

© 2022 The Authors. Small Structures published by Wiley-VCH GmbH. This is an open access article under the terms of the Creative Commons Attribution License, which permits use, distribution and reproduction in any medium, provided the original work is properly cited.

DOI: 10.1002/sstr.202200233

C. Chen, D. O'Hare
Chemistry Research Laboratory
Department of Chemistry
University of Oxford
12 Mansfield Road, Oxford OX1 3TA, UK

T. Zhou
State Key Laboratory of Structural Chemistry
Fujian Institute of Research on the Structure of Matter
Chinese Academy of Sciences
Fuzhou, Fujian 350002, P.R. China

Y. Zhou, Z. Zou
Jiangsu Key Laboratory for Nano Technology
National Laboratory of Solid State Microstructures
Collaborative Innovation Center of Advanced Microstructures
School of Physics
Nanjing University
Nanjing, Jiangsu 210093, P.R. China

R. Xu
C4T CREATE
National Research Foundation
CREATE Tower 1 Create Way
Singapore 138602, Singapore

the active sites besides their highly porous structures and large surface areas.[18] For example, MOFs have been used for CO_2 photoreduction with their large metal node as catalytic sites.[19–21]

In recent years, 2D or 3D COFs have received increasing interest in the field of heterogeneous photocatalysis,[22–27] due to their high solvent stability, extended π-conjugated framework for light harvesting and charge carrier transport, and open pore structures for mass transfer. Moreover, the columnar stacking of 2D-COFs can offer another channel system to facilitate charge carrier transport in the stacking direction besides the π-electron conjugation in-plane system, owing to the periodic columnar π-arrays of layered stacking of 2D polymer sheets.[28] Equally interesting, the inherent functional groups of the constituent ligands can be used to coordinate with metal cations to generate the molecular sites for catalysis. Single-atom catalysts (SACs) with isolated single metal atoms embedded within a solid matrix have been shown with enhanced activity for photocatalysis.[29] With all these, COFs serve as an excellent platform to construct and investigate SACs for challenging photochemical reactions, e.g., CO_2 photoreduction.

So far, there are two most commonly used moieties in COFs for metalation, namely, porphyrin in the node and bipyridine in the backbone for generation of Co, Cu, Zn, Ni, and Re based active sites for CO_2 photoreduction. Promising photocatalytic performances have been reported from these photocatalysts in the presence or absence of photosensitizers.[30–41] In addition, two more coordination sites were reported. The first one by Cooper and coworkers is iminopyridine moiety, which was shown as a promising alternative to bipyridine as metal coordination sites for CO_2 photoreduction.[41] Interestingly, the second one by Lan and coworkers is the interlayer quinone oxygen atoms of DQTP COF, which leads to the formation of O—M—O interlayer bonding as the active site.[32] Inspired by these findings, it will be worthwhile to explore more varieties of coordination sites given the abundant choice of COF ligands to design efficient photocatalysts for CO_2 reduction.

Herein, we used 2,5-dimethoxybenzene-1,4-dicarboxaldehyde (DHTA) and 4,4′,4″-(1,3,5-triazine-2,4,6-triyl)trianiline (TTA) to produce COF with relatively weak N and O binding sites from imine and methoxy groups of the ligands. Extensive characterization results indicate that Cu^{2+} can be anchored by both O and N sites to form a Cu–O/N active center for CO_2 reduction. The resultant 2D Cu–COF with 0.2 wt% Cu only serves as a bifunctional photocatalyst for visible-light-driven CO_2 reduction in the absence of a photosensitizer with triethanolamine (TEOA) as the sacrificial reagent. A high CO selectivity of 94% was obtained against H_2 production.

2. Results and Discussion

2.1. Properties of Cu–COF Photocatalyst

The synthesis method of Cu single site incorporated COF (Cu–COF) is shown in **Figure 1**a,b. Firstly, The DHTA-TTA

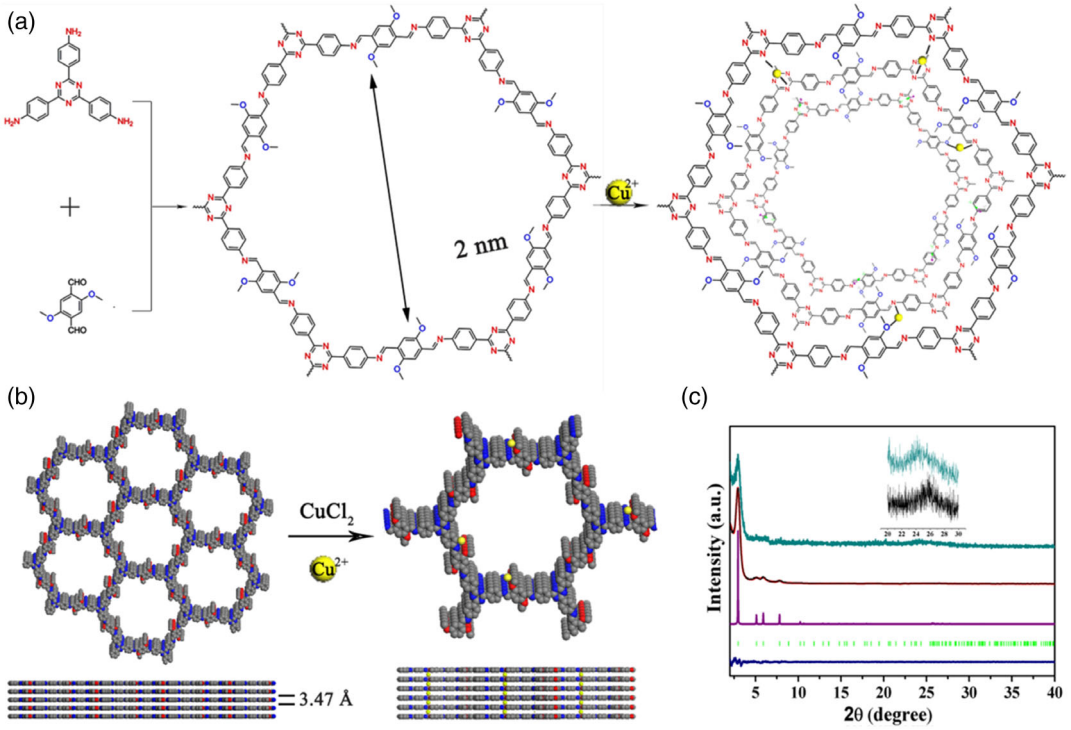


Figure 1. Preparation of 2D covalent organic framework (COF) photocatalyst with Cu–O/N single sites. a) Schematic representation of the synthesis of DHTA-TTA 2D COF and Cu–COF (Cu: yellow). b) Top (top) and side (bottom) views of DHTA-TTA 2D COF and Cu–COF structural models with eclipsed AA stacking structures (gray: carbon, blue: nitrogen, O: red, Cu: yellow, and H atoms are omitted for clarity). c) Experimental (black), Pawley-refined (red), simulated (purple, using AA stacking mode) powder X-ray diffraction (PXRD) and a difference plot for DHTA-TTA 2D COF, and PXRD patterns of Cu–COF obtained experimentally (dark cyan).

© 2022 The Authors. Small Structures published by Wiley-VCH GmbH

26884062, 2023, 6, Downloaded from https://onlinelibrary.wiley.com/doi/10.1002/sstr.202200233 by Test, Wiley Online Library on [19/07/2023]. See the Terms and Conditions (https://onlinelibrary.wiley.com/terms-and-conditions) on Wiley Online Library for rules of use; OA articles are governed by the applicable Creative Commons License

2D COF was obtained from the condensation of 2,5-dimethoxybenzene-1,4-dicarboxaldehyde (DHTA) and 4,4′,4″-(1,3,5-triazine-2,4,6-triyl)trianiline (TTA) in a sealed Pyrex tube by heating at 120 °C for 36 h. Subsequently, the solution of $CuCl_2$ dissolved in acetonitrile was added into COF-dispersed acetonitrile. Both mixtures are in yellow color before mixing. Interestingly, the color of the mixture of the two changed to red rapidly (Figure S1, Supporting Information), indicating the coordination of copper cations with COF. After stirring for 2 h and washing several times to remove the loosely adsorbed copper species, the dark yellow colored Cu–COF powder was obtained (Figure S1, Supporting Information). The percentage of Cu in Cu–COF was measured to be 0.2 wt% using inductively coupled plasma atomic emission spectrometry (ICP-AES). The low percentage of Cu is most probably due to the type of metalation sites, which will be discussed shortly.

The type of coordination between Cu cation and COF was first analyzed by Fourier transform infrared (FTIR) spectrum (Figure S2, Supporting Information). FTIR spectrum of COF shows the characteristic imine (C═N) vibration at 1625 cm^{-1} and the absence of the aldehyde stretching vibration at 1684 cm^{-1}, revealing the successful condensation between DHTA and TTA.[42] Furthermore, the stretch vibration of triazine units at 814 cm^{-1} is still present in the COF. However, there is no noticeable difference between the spectrum of Cu–COF and COF (Figure S3, Supporting Information), which is likely due to the very low percentage of Cu (0.2 wt%) in the sample. Therefore, other analytical techniques are required to prove the coordination between Cu and COF. The powder X-ray diffraction (PXRD) pattern of COF (Figure 1c) reveals the formation of a crystalline network with 2D honeycomb-type lattices as evidenced by the presence of an intense (100) diffraction at 2.92°. The smaller peaks at 5.08°, 5.87°, and 7.72° correspond to the (110), (200), and (210) diffraction, respectively. The magnified peak at 25.6° (the inset of Figure 1c) arises from the d-spacing between the (001) lattice planes, suggesting a typical van der Waals contact between the aromatic layers.[34] The structural simulation shows the most probable structure of COF with AA stacking mode. The XRD patterns from Pawley's refinement of the simulated structure is in good agreement with the experimental data, revealing the validity of the simulated model. The XRD result suggests that the COF possesses a 1D channel with a diameter of 2 nm, stacking along the c-axis with an interlayer distance of 3.47 Å. The weight percentage of C, H, and N contents measured with elemental analysis are 70.35%, 3.80%, and 15.23%, which are close to the theoretical values of 73.08%, 4.60%, and 14.20% of COF, indicating the successful formation of 2D COF.

Compared with pure COF, the XRD pattern of Cu–COF (Figure 1c) is maintained although the intensity of the peaks is generally decreased. This indicates that the structure of COF is retained, but the crystallinity is poorer. Interestingly, the peak corresponding to (001) lattice planes is shifted from 25.6° to 24.1° after metalation with Cu cations, corresponding to an expansion of the *d*-spacing from 3.47 to 3.69 Å. The enlarging of the *d*-spacing indicates that Cu cations are probably partially incorporated in the interlayer space.

As shown in **Figure 2**a and S4 and S5, Supporting Information, the transmission electron microscopy (TEM) images of COF and Cu–COF show a typical morphology of nanobelts with a length of 300–500 nm and a width of 20–50 nm. These nanobelts exhibit a smooth and clean surface, with no nanoclusters or nanoparticles observed on Cu–COF. Figure 2c shows the vertically standing nanobelts of COF with a thickness of 6–10 nm. The high-resolution TEM image (inset of Figure 2c)

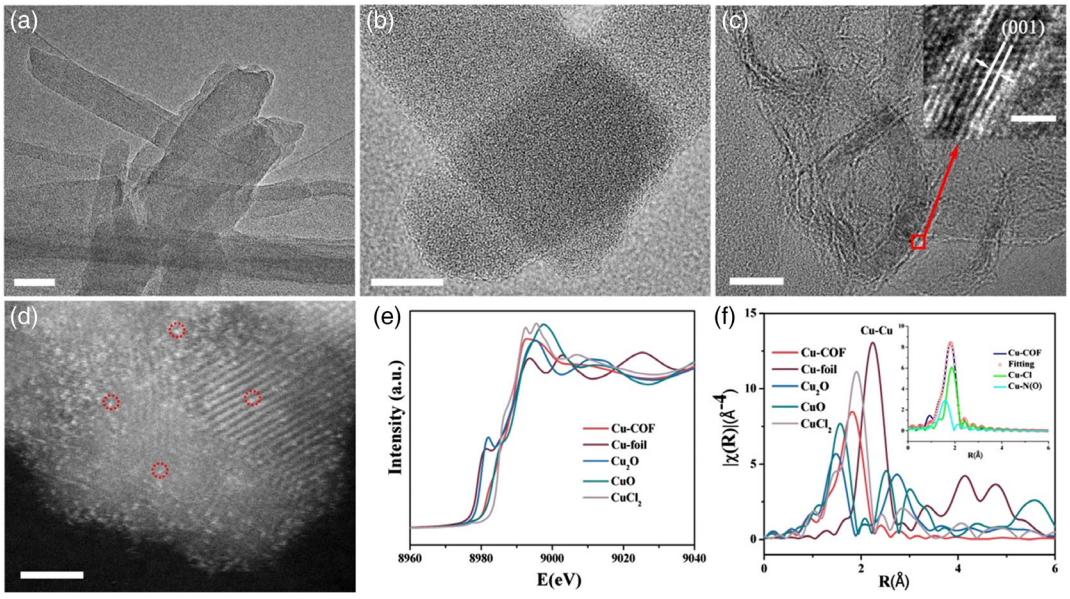


Figure 2. Structural characterization of COF and Cu-COF samples. a) Bright-field transmission electron microscopy (TEM) image and b) partial enlarged detail of flat-laying 2D COF. c) Bright-field TEM image of lateral 2D COF with selected high-resolution TEM (HRTEM) image. d) High-resolution high-angle annular dark-field scanning TEM (HAADF-STEM) image of Cu–COF. e) Normalized Cu *K*-edge X-ray absorption near edge structure (XANES) and f) the k_3-weighted Fourier-transform experimental extended X-ray absorption fine structure (EXAFS) spectra of the Cu–COF, Cu_2O, CuO, $CuCl_2$, and Cu Foil (inset: The EXAFS fitting results of Cu–COF).

© 2022 The Authors. Small Structures published by Wiley-VCH GmbH

26884062, 2023, 6, Downloaded from https://onlinelibrary.wiley.com/doi/10.1002/sstr.202200233 by Test, Wiley Online Library on [19/07/2023]. See the Terms and Conditions (https://onlinelibrary.wiley.com/terms-and-conditions) on Wiley Online Library for rules of use; OA articles are governed by the applicable Creative Commons License

reveals that the interplanar *d*-spacing between the well-defined lattice fringes in COF is 3.42 Å, corresponding to the *d*-spacing between the (001) lattice planes of COF, which is well consistent with the XRD results. To distinguish the Cu species with atomic resolution, the aberration-corrected high-angle annular dark-field scanning TEM (HAADF-STEM) was further performed. The bright spots corresponding to heavy Cu atoms are randomly dispersed on COF support (Figure 2d) and some of them were observed between the (001) lattice planes, confirming the XRD result that Cu atoms are partially incorporated in the interlayer space. Cu nanocluster or nanoparticle was not observed.

The nature of the Cu single sites was investigated by X-ray photoelectron spectroscopy (XPS) (Figure S6, Supporting Information) and X-ray absorption spectroscopy (Figure 2e,f). Compared to the N 1*s* spectrum of pure COF, besides the main peak at 398.5 eV which is attributed to C–N=C, a new shoulder peak located at a higher binding energy of 399.8 eV appears in the spectrum of Cu–COF,[43] confirming the formation of Cu—N bond with electron-donating effect from N to Cu species. On the other hand, the O 1*s* spectrum also shows an additional peak but at a lower binding energy of 531.6 eV compared to the main peak of O 1*s* in the methoxy group (533.1 eV). This indicates the formation of the Cu—O bond in Cu–COF. Based on the changes in the binding energy of N 1*s* and O 1*s* peak, it is highly likely that the N—Cu—O bond forms within the (001) plane or interlayer with electron redistributed from N to Cu to O. The Cu $2p_{3/2}$ peak at 932.8 eV in Cu 2*p* spectrum of Cu–COF can be assigned to Cu^{2+} in the Cu–COF,[44] indicating that there is no or minimal change of the oxidation state of Cu species after being incorporated in COF. The X-ray absorption fine structure (XAFS) measurements were performed to further investigate the local coordination environment of Cu in Cu–COF. The normalized Cu K-edge X-ray absorption near edge structure (XANES) spectrum of Cu–COF shows a higher energy position of the XANES edge than those of Cu foil and Cu_2O and a similar position to that of CuO (Figure 2e), confirming the Cu^{2+} oxidation state in Cu–COF. The experimental Fourier transform spectrum of Cu-COF from k^3-weighted normalized extended X-ray absorption fine structure (XAFS) result shows two fitted peaks, corresponding to the Cu—O/N bond and Cu—Cl bond (Figure 2f and Table S1, Supporting Information).[45,46] In reference to standard Cu foil, the peaks at 2.54 Å corresponding to the Cu—Cu bond appears in Cu foil, but are not observed in Cu–COF. These results suggest that the presence of isolated Cu atoms coordinates with adjacent O and N atoms in COF and Cl^- counter anions, which is in agreement with HAADF-STEM and XPS results. The curve fitting result of the XAFS spectrum reveals that the coordination numbers of the nearest-neighbor N (O) atoms and Cl atoms around the isolated Cu atom are 2 at 2 and 2.25 Å, respectively (Table S1, Supporting Information). Therefore, the XAFS results confirm isolated Cu atoms are coordinated with N (O) atoms in COF to form single sites on the COF surface,[47] which serve as the catalytic sites for CO_2 photoreduction.

The porosity of COF and Cu–COF was measured by nitrogen physisorption method. The nitrogen adsorption–desorption isotherms of COF and Cu–COF display typical type IV curves with an H3 hysteresis loop, indicating the presence of mesopores (**Figure 3**a). The Brunauer–Emmett–Teller (BET) surface area

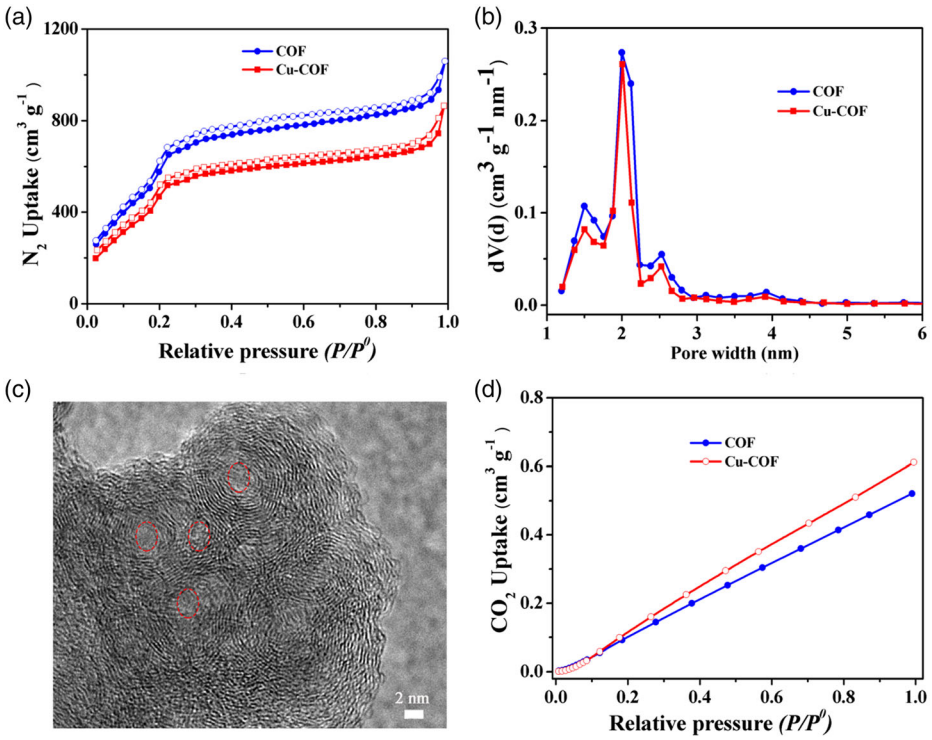


Figure 3. Porous structure and gas adsorption of COF and Cu–COF. a) Nitrogen adsorption isotherm (filled symbols) and desorption isotherm (open symbols) of COF and Cu–COF at 77.3 K. b) Pore size distribution of COF and Cu–COF. c) HRTEM image of COF with an average pore diameter of around 2.0 nm. d) CO_2 adsorption isotherms of COF and Cu–COF.

© 2022 The Authors. Small Structures published by Wiley-VCH GmbH

26884062, 2023, 6, Downloaded from https://onlinelibrary.wiley.com/doi/10.1002/sstr.202200233 by Test, Wiley Online Library on [19/07/2023]. See the Terms and Conditions (https://onlinelibrary.wiley.com/terms-and-conditions) on Wiley Online Library for rules of use; OA articles are governed by the applicable Creative Commons License

of COF and Cu–COF was determined to be 2287 and 1888 $m^2 g^{-1}$, respectively. The slight decrease in the BET surface area should result from the anchoring of Cu species on COF. The pore size distribution of COF and Cu–COF (Figure 3b) displays a narrow pore width distribution centered at around 2 nm, which is in excellent agreement with the pore size established from the structural analysis and simulation. The high-resolution TEM image of COF (Figure 3c) also confirms the pore size of around 2.0 nm. Figure 3d shows the CO_2 adsorption isotherms of COF and Cu–COF. The amount of CO_2 absorbed by the COF and Cu–COF under ambient pressure at 25° is 0.521 and 0.612 mmol g^{-1}, respectively. The CO_2 adsorption capacity of Cu–COF is slightly higher than that of COF despite the lower BET surface area of Cu–COF, revealing that the Cu—O/N bonds in COF benefit CO_2 chemisorption.

2.2. Photocatalytic CO_2 Reduction and Stability

The catalytic performance of Cu–COF for photocatalytic CO_2 reduction reaction was evaluated in acetonitrile/water mixture using TEOA as the sacrificial electron donor under visible light irradiation (>420 nm). First of all, as shown in **Figure 4**a, the control experiments carried out in the absence of light, CO_2, TEOA, or photocatalyst did not give any activity. With Cu–COF, CO_2 can be selectively reduced to CO in the absence of any photosensitizer. The average CO evolution rate over 5 h is 206 μmol $g^{-1} h^{-1}$. The selectivity of CO over H_2 is as high as 94% with an H_2 evolution rate of 14 μmol $g^{-1} h^{-1}$. No liquid hydrocarbon products such as CH_3OH and HCHO were detected (Figure S7, Supporting Information). For comparison, COF itself exhibits a much lower activity and selectivity for CO evolution at 30 μmol $g^{-1} h^{-1}$ and a selectivity of 40%, respectively. The turnover frequency (TO/F) per Cu site of Cu–COF is 6.5 h^{-1}. When an equivalent amount of $CuCl_2$ (0.2 wt% of Cu) was added in situ during the photoreaction, the CO TOF of the sample (0.2Cu^{2+} COF) is only 1.6 h^{-1}. It is believed that in this case most of Cu^{2+} was present as the homogenous co-catalyst in the solution, giving rise to a low CO selectivity to H_2 as well besides the low activity. When more $CuCl_2$ (2 wt% of Cu) was added in situ (2Cu^{2+} COF), both CO and H_2 evolution rates increase to 154 and 80 μmol $g^{-1} h^{-1}$, respectively. After the reaction, numerous Cu nanoparticles of <5 nm were found on COF nanobelts (Figure S8, Supporting Information). Though the formation of a Cu single site cannot be excluded in this sample, it is believed that Cu nanoparticles are also an active catalyst for H_2 evolution, resulting in a lower CO selectivity of 66%. Though it is hard to directly compare the performance of various COF–M photocatalysts due to different reaction conditions as shown in Table S2, Supporting Information, Cu–O/N site with only 0.2 wt% of Cu in our COF shows at least comparable if not better

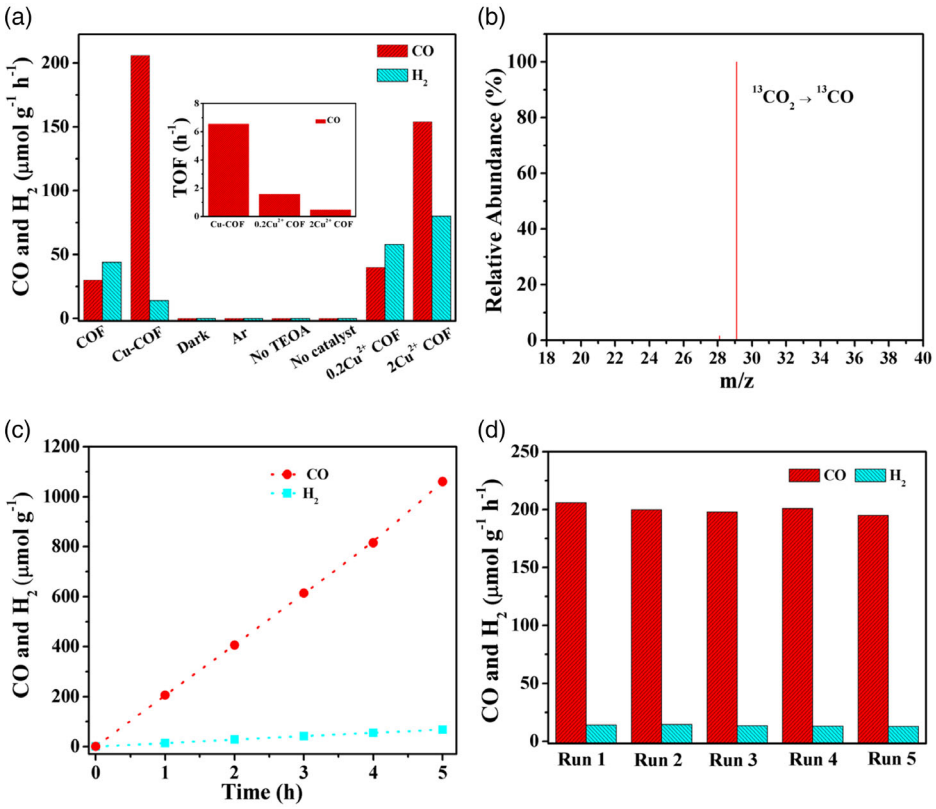


Figure 4. Photocatalytic CO_2 reduction performance of samples. a) CO and H_2 evolution rate over COF and Cu–COF under visible-light ($\lambda > 420$ nm) irradiation, in comparison with that of COF with 0.2 and 2 wt% Cu^{2+} added in situ during the photoreaction under the same reaction condition (inset: the calculated TOF of Cu–COF, 0.2Cu^{2+} COF, and 2Cu^{2+} COF). b) GC-MS results of ^{13}CO produced over Cu–COF from $^{13}CO_2$ isotope experiment. c) Time course of CO and H_2 evolution over Cu–COF. d) CO and H_2 evolution rate in stability tests over Cu–COF with 5 h for each run.

© 2022 The Authors. Small Structures published by Wiley-VCH GmbH

26884062, 2023, 6, Downloaded from https://onlinelibrary.wiley.com/doi/10.1002/sstr.202200233 by Test, Wiley Online Library on [19/07/2023]. See the Terms and Conditions (https://onlinelibrary.wiley.com/terms-and-conditions) on Wiley Online Library for rules of use; OA articles are governed by the applicable Creative Commons License

performance with other active sites including Co, Ni, Zn, and Re sites incorporated with porphyrin and/or dipyridine.

To validate the source of the generated CO, an isotopic experiment using $^{13}CO_2$ as feedstock was performed under the same reaction condition. A major signal at $m/z = 29$ corresponding to ^{13}CO appears (Figure 4b), demonstrating that the as-detected CO truly originates from the CO_2 gas source. After photoreaction for 5 h (Figure 4c), the total product of CO reached 1060 μmol g^{-1} h^{-1}. As shown in Figure 4d, the activity and selectivity of Cu–COF have no evident deactivation within 5 recycle runs, showing the excellent stability of Cu–COF. The XRD pattern (Figure S9, Supporting Information) of Cu–COF after photoreaction shows no obvious change, indicating the structure of COF is stable. In addition, no Cu-derived nanoclusters or nanoparticles were observed over Cu–COF after photoreaction (Figure S10, Supporting Information) showing that Cu–O/N single sites in COF are highly stable under photocatalytic CO_2 reduction conditions.

2.3. Reaction Mechanism

The photocatalytic performance is determined by the balance of thermodynamics and kinetics of light harvesting, charge transport and separation, and catalytic reaction processes. The UV−visible absorption spectrum (**Figure 5**a) reveals that COF alone already exhibits strong visible light absorption with an absorption edge at around 512 nm, corresponding to a bandgap energy of 2.42 eV (Figure S11a, Supporting Information). After incorporation with Cu, the absorption edge of Cu–COF is red-shifted to 527.6 nm corresponding to a slightly narrower band gap energy of 2.35 eV. In addition, enhanced visible light absorption up to 800 nm is observed for Cu–COF due to increased delocalization with the metalation of Cu.[32,38] According to the XPS valence band (VB) spectra (Figure S11b, Supporting Information), the VB maximum position of COF and Cu–COF is located at 1.65 and 1.53 eV, respectively. Thus, the conduction band (CB) position of COF and Cu–COF is derived as –0.77 and –0.82 eV, respectively. The CB edge of COF and Cu–COF is more negative than E^o (CO/CO_2) ($CO_2 + 2e^- + 2\,H^+ \rightarrow CO + H_2O$, $E^o_{redox} = -0.53$ V versus NHE, pH 7) possessing the sufficient driving force the CO_2 photoreduction to CO.

To explore the charge transfer between COF and Cu, the photoluminescence (PL) transient time-resolved decay measurements were carried out on the samples excited at 301 nm (Figure 5b). Cu–COF displays PL decay lifetime of 0.81 ns, faster than 1.28 ns of the pure COF, implying an additional nonradiative decay channel through the transfer of electrons from COF to Cu–O/N sites. The electron-transfer rate from COF to Cu calculated using the equation in the form of

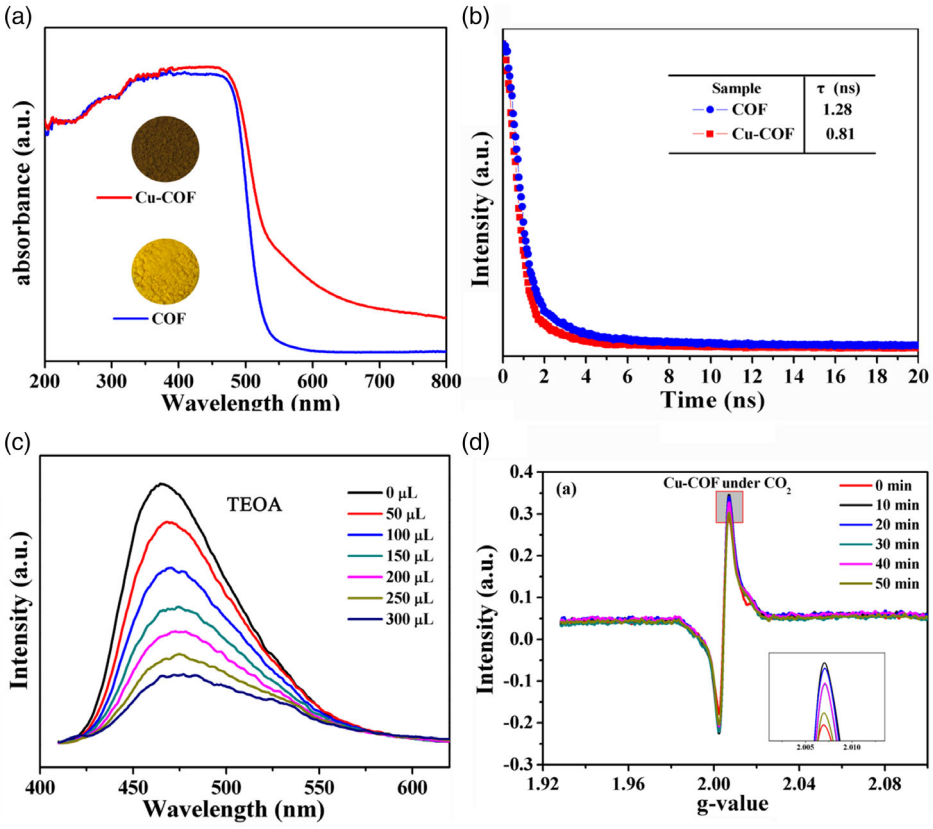


Figure 5. Spectroscopic evidence insights into photocatalytic CO_2 reduction over Cu–COF. a) UV–visible absorption spectra of COF and Cu–COF, and the photographs of the samples (the inset). b) The photoluminescence (PL) decay traces of COF and Cu–COF. c) Fluorescence spectra of Cu–COF with the addition of different amounts of triethanolamine (TEOA) ($\lambda_{ex} = 400$ nm). d) In situ electron paramagnetic resonance (EPR) spectra of Cu–COF under different light irradiation times).

© 2022 The Authors. Small Structures published by Wiley-VCH GmbH

26884062, 2023, 6, Downloaded from https://onlinelibrary.wiley.com/doi/10.1002/sstr.202200233 by Test, Wiley Online Library on [19/07/2023]. See the Terms and Conditions (https://onlinelibrary.wiley.com/terms-and-conditions) on Wiley Online Library for rules of use; OA articles are governed by the applicable Creative Commons License

26884062, 2023, 6, Downloaded from https://onlinelibrary.wiley.com/doi/10.1002/sstr.202200233 by Test, Wiley Online Library on [19/07/2023]. See the Terms and Conditions (https://onlinelibrary.wiley.com/terms-and-conditions) on Wiley Online Library for rules of use; OA articles are governed by the applicable Creative Commons License

$k_{et} = 1/\tau(\text{Cu–COF}) - 1/\tau(\text{COF})$[48] is $0.45 \times 10^{-9}\ s^{-1}$, indicating fast transfer of electrons from COF to Cu atoms via Cu—O/N bonds. These results together with high CO_2 uptake capacity in Cu–COF explain the improved photoreduction efficiency of CO_2 to CO. The PL quenching experiments with the addition of TEOA in a degassed solution of CH_3CN/H_2O (v:v = 4:1) were also performed to investigate the photocatalytic mechanism (Figure 5c). The fluorescence intensity of Cu–COF gradually decreases with the increase of the amount of TEOA, owing to the oxidative quenching of photogenerated holes from Cu–COF via TEOA.[49] It is revealed that TEOA serves as a sacrificial reagent to consume photogenerated holes from Cu–COF for CO_2 photoreduction.

To further investigate the photocatalytic process of CO_2 reduction, in situ electron paramagnetic resonance (EPR) experiments were carried out under the dark or visible light irradiation condition. Compared to the weak signals of COF (Figure S12, Supporting Information), Cu–COF exhibits a narrow isotropic signal with Lorentzian line shape at $g = 2.008$, showing that Cu—O/N sites bonded on COF increase the spin–spin interaction from the stacking of aromatic layers in COF. The g signals of Cu–COF obviously increase in the CO_2 atmosphere with 10 min of light irradiation (Figure 5c and S13, Supporting Information), revealing that the Cu–O/N sites benefit the electron separation upon photoexcitation. After 10 min of light irradiation, the EPR signals gradually decrease with irradiation time, because the adsorption of CO_2 molecules reaches equilibrium on the Cu–O/N sites and consume the electron for CO_2 reduction. The in situ EPR tests were also conducted over COF (Figure S14, Supporting Information) and $CuCl_2$ (Figure S15, Supporting Information) in the CO_2 and N_2 atmosphere. Such changes in the signals were not observed. Therefore, the aforementioned results imply that the Cu–O/N sites can improve the conversion effciency of CO_2 photoreduction.

3. Conclusions

In summary, a new single-site heterogeneous photocatalyst has been constructed by incorporating isolated Cu atoms on the linkers of 2D COF ultrathin nanobelts. The formation of Cu–O/N single sites were confirmed by complementary analytical results. The Cu–COF serves as an efficient bifunctional photocatalyst for visible-light-driven CO_2 reduction to CO with 94% selectivity. The mechanistic study by in situ EPR confirms that the Cu–O/N sites benefit the electron transfer from COF upon photoirradiation and serve as the active sites for highly selective reduction of CO_2 to CO. This work demonstrates the potential of COFs as photocatalysts for CO_2 conversion and beyond.

4. Experimental Section

Materials: 2,5-dimethoxybenzene-1,4-dicarboxaldehyde, 4-aminobenzonitrile, trifluoromethanesulfonic acid were purchased from Sigma-Aldrich. Chloroform, N-methyl-2-pyrrolidone (NMP), 1,2-dichlorobenzene, and 1-butanol, tetrahydrofuran (THF) were obtained from VWR. All chemicals were used as received without further purification. 4,4′,4″-(1,3,5-Triazine-2,4,6-triyl)trianiline was synthesized following a previously reported method.[42] Anhydrous copper (II) chloride ($CuCl_2$) was purchased from Sigma-Aldrich. Deionized water was used in all experiments.

Synthesis of COF: A Pyrex tube (25 mL) was charged with 4,4′,4″-(1,3,5-triazine-2,4,6-triyl)trianiline (0.48 mmol, 0.1702 g), 2,5-dimethoxybenzene-1,4-dicarboxaldehyde (0.72 mmol, 0.1398 g), 1,2-dichlorobenzene (3 mL), 1-butanol (3 mL), and 6 M aqueous acetic acid (0.6 mL). The tube was flash frozen at a liquid N_2 bath, degassed by three freeze–pump–thaw cycles, and then sealed off. After being warmed to room temperature, the mixture was sonicated for 2 min, and then heated at 120 °C for 36 h in an oil bath. The yellow-colored precipitate was collected by centrifugation, washed thoroughly with THF, and dried in a vacuum oven at 60 °C for 24 h.

Synthesis of Cu–COF: COF (10 mg) and $CuCl_2$ (5 mg) were separately added into acetonitrile (25 mL) and the mixtures were ultrasonicated for 10 min. Afterward, they were mixed. Upon mixing, the color of the mixture turned from yellow to red immediately. The mixture was continuously stirred for 2 h at room temperature. The resulting Cu–COF was filtered, washed with excess acetonitrile and water, and dried by lyophilization.

Characterization: The crystal structure of the as-prepared samples was characterized by PXRD (Bruker) equipped with Cu Kα radiation. FTIR spectra were obtained with a PerkinElmer FTIR Spectrum GX using the KBr technique in the range of 4000–400 cm^{-1}. Elemental analysis for carbon and nitrogen was performed on a Vario EL III Element analyzer. The specific surface area of the samples was measured by nitrogen sorption at 77 K on a surface area and porosity analyzer (Quantachrome Autosorb-6B). The samples were degassed at 120 °C for 16 h under vacuum before the analysis. The morphology of the samples was observed by transmission electron microscopy (TEM, JEOL 3010). Atomic HAADF-STEM characterization was conducted on a probe-corrected JEOL JEM-ARM200F STEM. ICP-AES was carried out on a Perkin-Elmer ICP Optima 2000DV instrument. The Cu K-edge XANES and extended X-ray absorption fine structure (EXAFS) spectra were recorded at the 1W2B beamline of the Beijing synchrotron radiation facility (BSRF). XPS analysis was conducted on an AXIS-HSi spectroscope (Kratos Analytical) using a monochromated Al Kα X-ray source (1486.7 eV), and the binding energy was calibrated using the C1*s* peak at 284.6 eV. The UV–visible absorption spectra were obtained on a UV-2450 spectrophotometer (Shimadazu) at room temperature. The transient time-resolved PL decay measurements were conducted on a spectrophotometer (PL, He-Cd laser, LabramHR800). PL spectra were collected on a Fluoromax-3 spectrometer (Horiba Scienti fic) at room temperature. The in situ EPR data were obtained on a BRUKER BIOSPIN AVANCE III 400 MHz spectrometer, during which samples in solution (CH_3CN/H_2O: 4:1) were tested with N_2 or CO_2 under visible-light irradiation or without light. The nuclear magnetic resonance data was tested on Bruker Avance III 400 (BBFO 400).

Photocatalysis Measurement of CO_2 Reduction Reactions: The visible-light-driven photocatalytic CO_2 reduction was conducted in a closed gas circulation and evacuation system fitted with a top window Pyrex cell. A circulating cooling water system was used to maintain the reactor at around 20 °C. In a typical reaction, 5 mg of the catalyst (for each test) and 2 mL of TEOA were added to 10 mL of acetonitrile/H_2O solvent mixture with a volume ratio of 4/1 (CH_3CN/H_2O). A 300 W xenon lamp equipped with a 420 nm cutoff filter (Newport) was used as the visible light source. Before light irradiation, the reaction system was evacuated and refilled with high-purity CO_2 (99.995%; SOXAL) several times to remove the air inside and finally filled with CO_2 gas to a pressure of 600 torr. The evolved gas was detected by online GC (Agilent 7890 A) equipped with a thermal conductivity detector and a flame ionization detector (FID) at different durations of the photoreaction. To evaluate catalyst reusability, the samples were collected by centrifugation and reused again in a fresh solution.

The $^{13}CO_2$ isotope tracer experiment was performed under the same photocatalytic reaction condition except that the photoreactor was filled with $^{13}CO_2$ gas (99 at% ^{13}C; Aldrich) to a pressure of 400 torr before the light was turned on. After 4 h of irradiation, 250 µL of product gas was withdrawn using a gas-tight syringe and then injected into a GC-MS (Agilent, GC Model 6890N/MS Model 5973) with a molecular sieve 5 Å column for analysis.

© 2022 The Authors. Small Structures published by Wiley-VCH GmbH

Supporting Information

Supporting Information is available from the Wiley Online Library or from the author.

Acknowledgements

This work is supported by Nanyang Technological University and the National Research Foundation (NRF), Singapore, under its Campus for Research Excellence and Technological Enterprise (CREATE) program through the Carbon Reduction in Chemical Technology (C4T) program. Dr. W.T. and Prof. Z.Z. gratefully acknowledge the support by the Program from Guangdong Introducing Innovative and Entrepreneurial Teams (2019ZT08L101 and RCTDPT-2020-001), the University Development Fund (UDF01001159), the Shenzhen Key Laboratory of Eco-materials and Renewable Energy (ZDSYS20200922160400001), the Young Scientists Fund of the National Natural Science Foundation of China (Grant No. 52202306), and the Shenzhen Natural Science Foundation (GXWD20201231105722002-20200824163747001). The authors would like to express their gratitude to Neil Young and IanGriffiths who support them to use JEOL ARM-200F in the David Cockayne Centre for Electron Microscopy, University of Oxford.

Conflict of Interest

The authors declare no conflict of interest.

Data Availability Statement

The data that support the findings of this study are available from the corresponding author upon reasonable request.

Keywords

CO_2 reduction reactions, Cu–O/N single sites, single-atom catalysts, 2D covalent organic frameworks, ultrathin nanobelts

Received: August 30, 2022
Revised: September 22, 2022
Published online: October 14, 2022

[1] T. Inoue, A. Fujishima, S. Konishi, K. Honda, *Nature* **1979**, *277*, 637.
[2] M. R. Hoffmann, J. A. Moss, M. M. Baum, *Dalton Trans.* **2011**, *40*, 5151.
[3] W. G. Tu, Y. Zhou, Z. G. Zou, *Adv. Mater.* **2014**, *26*, 4607.
[4] J. L. White, M. F. Baruch, J. E. Pander, Y. Hu, I. C. Fortmeyer, J. E. Park, T. Zhang, K. Liao, J. Gu, Y. Yan, T. W. Shaw, E. Abelev, A. B. Bocarsly, *Chem. Rev.* **2015**, *115*, 12888.
[5] S. N. Habisreutinger, L. Schmidt-Mende, J. K. Stolarczyk, *Angew. Chem., Int. Ed.* **2013**, *52*, 7372.
[6] J. G. Yu, J. X. Low, W. Xiao, P. Zhou, M. Jaroniec, *J. Am. Chem. Soc.* **2014**, *136*, 8839.
[7] S. Neatu, J. A. Macia-Agullo, P. Concepcion, H. Garcia, *J. Am. Chem. Soc.* **2014**, *136*, 15969.
[8] W. G. Tu, Y. Zhou, H. J. Li, P. Li, Z. G. Zou, *Nanoscale* **2015**, *7*, 14232.
[9] M. F. Kuehnel, K. L. Orchard, K. E. Dalle, E. Reisner, *J. Am. Chem. Soc.* **2017**, *139*, 7217.
[10] M. Zhou, S. B. Wang, P. J. Yang, C. J. Huang, X. C. Wang, *ACS Catal* **2018**, *8*, 4928.
[11] S. B. Wang, X. C. Wang, *Appl. Catal., B* **2015**, *162*, 494.
[12] Q. Liu, Y. Zhou, J. H. Kou, X. Y. Chen, Z. P. Tian, J. Gao, S. C. Yan, Z. G. Zou, *J. Am. Chem. Soc.* **2010**, *132*, 14385.
[13] Q. Liu, Y. Zhou, Z. P. Tian, X. Y. Chen, J. Gao, Z. G. Zou, *J. Mater. Chem.* **2012**, *22*, 2033.
[14] Y. F. Xu, M. Z. Yang, B. X. Chen, X. D. Wang, H. Y. Chen, D. B. Kuang, C. Y. Su, *J. Am. Chem. Soc.* **2017**, *139*, 5660.
[15] M. Ou, W. Tu, S. Yin, W. Xing, S. Wu, H. Wang, S. Wan, Q. Zhong, R. Xu, *Angew. Chem., Int. Ed.* **2018**, *130*, 13758.
[16] X. X. Chang, T. Wang, J. L. Gong, *Energy Environ. Sci.* **2016**, *9*, 2177.
[17] H. Tong, S. X. Ouyang, Y. P. Bi, N. Umezawa, M. Oshikiri, J. H. Ye, *Adv. Mater.* **2012**, *24*, 229.
[18] W. G. Tu, Y. Xu, S. M. Yin, R. Xu, *Adv. Mater.* **2018**, *30*, 1707582.
[19] L. L. Ling, W. J. Yang, P. Yan, M. Wang, H. L. Jiang, *Angew. Chem., Int. Ed.* **2022**, *61*, e202116396.
[20] S. Wang, X. Wang, *Small* **2015**, *11*, 3097.
[21] J. Li, H. Huang, W. Xue, K. Sun, X. Song, C. Wu, L. Nie, Y. Li, C. Liu, Y. Pan, H. L. Jiang, D. Mei, C. Zhong, *Nat. Catal.* **2021**, *4*, 719.
[22] V. S. Vyas, F. Haase, L. Stegbauer, G. Savasci, F. Podjaski, C. Ochsenfeld, B. V. Lotsch, *Nat. Commun.* **2015**, *6*, 8508.
[23] H. X. Lin, C. P. Chen, T. H. Zhou, J. Zhang, *Sol. RRL* **2021**, *5*, 2000458.
[24] H. Wang, H. Wang, Z. Wang, L. Tang, G. Zeng, P. Xu, M. Chen, T. Xiong, C. Zhou, X. Li, D. Huang, Y. Zhu, Z. Wang, J. Tang, *Chem. Soc. Rev.* **2020**, *49*, 4135.
[25] H. Wang, C. Qian, J. Liu, Y. Zeng, D. Wang, W. Zhou, L. Gu, H. Wu, G. Liu, Y. L. Zhao, *J. Am. Chem. Soc.* **2020**, *142*, 4862.
[26] Z. A. Lan, Y. X. Fang, Y. F. Zhang, X. C. Wang, *Angew. Chem., Int. Ed.* **2018**, *57*, 470.
[27] S. Y. Ding, J. Gao, Q. Wang, Y. Zhang, W. G. Song, C. Y. Su, W. Wang, *J. Am. Chem. Soc.* **2011**, *133*, 19816.
[28] Y. F. Zhi, Z. R. Wang, H. L. Zhang, Q. C. Zhang, *Small* **2020**, *16*, 2001070.
[29] C. Gao, J. X. Low, R. Long, T. T. Kong, J. F. Zhu, Y. J. Xiong, *Chem. Rev.* **2020**, *120*, 12175.
[30] H. Nguyen, A. Alzamly, *ACS Catal.* **2021**, *11*, 9809.
[31] Y. R. Wang, H. M. Ding, X. Y. Ma, M. Liu, Y. Yang, Y. Chen, S. Li, Y. Lan, *Angew. Chem., Int. Ed.* **2022**, *61*, e202200003.
[32] M. Lu, Q. Li, J. Liu, F.-M. Zhang, L. Zhang, J.-L. Wang, Z.-H. Kang, Y.-Q. Lan, *Appl. Catal., B* **2019**, *254*, 624.
[33] W. Liu, X. Li, C. Wang, H. Pan, W. Liu, K. Wang, Q. Zeng, R. Wang, J. Jiang, *J. Am. Chem. Soc.* **2019**, *141*, 17431.
[34] Y.-N. Gong, W. Zhong, Y. Li, Y. Qiu, L. Zheng, J. Jiang, H.-L. Jiang, *J. Am. Chem. Soc.* **2020**, *142*, 16723.
[35] H. Lv, R. Sa, P. Li, D. Yuan, X. Wang, R. Wang, *Sci. China Chem.* **2020**, *63*, 1289.
[36] M. Lu, J. Liu, Q. Li, M. Zhang, M. Liu, J.-L. Wang, D.-Q. Yuan, Y.-Q. Lan, *Angew. Chem., Int. Ed.* **2019**, *58*, 12392.
[37] W. Zhong, R. Sa, L. Li, Y. He, L. Li, J. Bi, Z. Zhuang, Y. Yu, Z. Zou, *J. Am. Chem. Soc.* **2019**, *141*, 7615.
[38] S. Yang, W. Hu, X. Zhang, P. He, B. Pattengale, C. Liu, M. Cendejas, I. Hermans, X. Zhang, J. Zhang, J. Huang, *J. Am. Chem. Soc.* **2018**, *140*, 14614.
[39] Z. Fu, X. Wang, A. M. Gardner, X. Wang, S. Y. Chong, G. Neri, A. J. Cowan, L. Liu, X. Li, A. Vogel, R. Clowes, M. Bilton, L. Chen, R. S. Sprick, A. I. Cooper, *Chem. Sci.* **2020**, *11*, 543.
[40] S. Li, S. Meng, X. Zou, M. El-Roz, I. Telegeev, O. Thili, T. Liu, G. Zhu, *Microporous Mesoporous Mater.* **2019**, *285*,, 195.
[41] X. Wang, Z. Fu, L. Zheng, C. Zhao, X. Wang, S. Y. Chong, F. McBride, R. Raval, M. Bilton, L. Liu, X. Wu, L. Chen, R. S. Sprick, A. I. Cooper, *Chem. Mater.* **2020**, *32*, 9107.

© 2022 The Authors. Small Structures published by Wiley-VCH GmbH

26884062, 2023, 6, Downloaded from https://onlinelibrary.wiley.com/doi/10.1002/sstr.202200233 by Test, Wiley Online Library on [19/07/2023]. See the Terms and Conditions (https://onlinelibrary.wiley.com/terms-and-conditions) on Wiley Online Library for rules of use; OA articles are governed by the applicable Creative Commons License

[42] D. Mullangi, S. Shalini, S. Nandi, B. Choksi, R. Vaidhyanathan, *J. Mater. Chem. A* **2017**, *5*, 8376.
[43] J. Feng, L. Zheng, C. Jiang, Z. Chen, L. Liu, S. Zeng, L. Bai, S. Zhang, X. Zhang, *Green Chem.* **2021**, *23*, 5461.
[44] T. Zhang, D. Zhang, X. Han, T. Dong, X. Guo, C. Song, R. Si, W. Liu, Y. Liu, Z. Zhao, *J. Am. Chem. Soc.* **2018**, *140*, 16936.
[45] A. Nimmermark, L. Ohrstrom, J. Reedijk, *Z. Krist-Cryst. Mater.* **2013**, *228*, 311.
[46] Z. Weng, Y. S. Wu, M. Y. Wang, J. B. Jiang, K. Yang, S. J. Huo, X. F. Wang, Q. Ma, G. W. Brudvig, V. S. Batista, Y. Y. Liang, Z. X. Feng, H. L. Wang, *Nat. Commun.* **2018**, *9*, 415.
[47] Y. Cai, J. Fu, Y. Zhou, Y.-C. Chang, Q. Min, J.-J. Zhu, Y. Lin, W. Zhu, *Nat. Commun.* **2021**, *12*, 586.
[48] G. Williams, P. V. Kamat, *Langmuir* **2009**, *24*, 13869.
[49] Z.-Y. Zhu, Q.-Q. Yang, L.-F. Gao, L. Zhang, A.-Y. Shi, C.-L. Sun, Q. Wang, H.-L. Zhang, *J. Phys. Chem. Lett.* **2017**, *8*, 1610.

© 2022 The Authors. Small Structures published by Wiley-VCH GmbH

26884062, 2023, 6, Downloaded from https://onlinelibrary.wiley.com/doi/10.1002/sstr.202200233 by Test, Wiley Online Library on [19/07/2023]. See the Terms and Conditions (https://onlinelibrary.wiley.com/terms-and-conditions) on Wiley Online Library for rules of use; OA articles are governed by the applicable Creative Commons License